Adv Polym Sci (2005) 182: 131–169
DOI 10.1007/b135562

Published online: 26 July 2005

Nano-Imaging of Polymers by Optical Microscopy

Shinzaburo Ito (✉) · Hiroyuki Aoki

Department of Polymer Chemistry, Graduate School of Engineering,
Kyoto University, Katsura, 615-8510 Kyoto, Japan
sito@photo.polym.kyoto-u.ac.jp

Abstract The developments of laser scanning confocal microscopy (LSCM) and scanning near-field optical microscopy (SNOM) have expanded the application range of optical microscopy from micron to nanometer dimensions, in which the molecular and macromolecular materials exhibit intrinsic fundamental characteristics closely related to their functionality. Although atomic force and electron microscopes have often been utilized for observing materials in nanometer dimensions, the world of the critical length (10–100 nm) of nano-technology and science is now illuminated by "light", and is revealed as real optical images from different points of view associated with not only morphology but also spectroscopic, analytical, time-resolved and opto-electrical responses in a local space. This article reviews the recent findings made by LSCM and SNOM mainly in terms of morphology of polymeric materials; particular concerns are in the phase-separated structures of polymer blends, conformation and morphology of a single polymer chain, and also two-dimensional ultra-thin polymer films. These optical techniques will become an indispensable tool for understanding molecular and biological systems.

Keywords Scanning near-field optical microscopy (SNOM) · Laser scanning conforcal microscopy (LSCM) · Fluorescence spectroscopy · Single polymer chain · Nano-structure

Abbreviations

AFM	atomic force microscopy
BAM	Brewster angle microscopy
BS	beam splitter
DNA	deoxyribonucleic acid
DUV	deep ultraviolet
Eo	eosin
FWHM	full width at half maximum
IPN	interpenetrating polymer network
LB	Langmuir-Blodgett
LSCM	laser scanning confocal microscopy
LSCFM	laser scanning confocal fluorescence microscopy
NA	numerical aperture
OM	optical microscopy
PB	polybutadiene
PDF	poly(9,9-dialkylfluorene)
Pe	perylene
PiBMA	poly(isobutyl methacrylate)
PMMA	poly(methyl methacrylate)
PODMA	poly(octadecyl methacrylate)
PPV	poly(*p*-phenylenevinylene)
PS	polystyrene
Py	pyrene
R6G	rhodamine-6G
SBR	poly(styrene-*ran*-butadiene)
SD	spinodal decomposition
SEM	scanning electron microscopy
SNOM	scanning near-field optical microscopy
STED	stimulated emission depletion
SWNT	single wall carbon nanotube
TEM	transmission electron microscopy
TIR	total internal reflection

1 Introduction

Optical microscopy (OM) has played essential roles in science, particularly for biological and medical research. This is due to the great advantage of OM; that is, real images of materials are easily observable at an ambient temperature and the atmospheric pressure, although the spatial resolution is limited to a micron scale due to the diffraction of light. In spite of a low magnification, optical techniques have reserved indispensable positions so far when the

objectives are so-called "soft materials" such as cells, micelles, membranes and a variety of organic molecular assemblies. This is also the case for observation of polymeric materials. Electron microscopes such as TEM and SEM have been widely employed for studying morphology of polymers, because the real space images provide unambiguous evidence on nano-structures of various polymer systems with a high resolution. Although it is often very hard for the samples to be selectively stained and to withstand the severe irradiation of electron beams in vacuo, the information obtained by the real images is superior to that from scattering methods using light, neutron, and X-ray etc., in particular for studying amorphous polymers. The growing interest in recent years in nano-science and technology has raised strong demands on nano-imaging in real space, and many researchers in materials science have awaited the developments of high resolution and convenient OM, applicable to soft materials and polymers. Here, we review the rapid progress made in the last decade on nano-imaging of polymer samples mainly by laser scanning confocal microscopy and scanning near field optical microscopy.

2
Nano-Imaging with Laser Scanning Confocal Microscopy

2.1
Instruments

Laser scanning confocal microscopy (LSCM) has been developed as a novel microscopic instrument, possessing the full merits of the optical techniques mentioned above. It is a kind of scanning microcopy technique that measures only one point in an object at a time by focusing the laser light on the small volume and scans it point by point to make an image [1, 2], whereas a conventional microscope can obtain an entire image of an object in the field of view at once. Figure 1a shows a typical optical system for confocal microscopy. The light from a point source is focused by an objective lens to illuminate a small point in the object. The optical response such as scattering, reflection, and fluorescence from the point illuminated, is collected by the same lens, and its intensity is measured by a photo-detector equipped with a pinhole. The confocal pinhole acts as a spatial filter for the selective detection of signals from the focal point, resulting in enhancement of the image contrast and improvement of the spatial resolution. The presence of the confocal pinhole is effective especially in improving the resolution in the depth direction. The stray light from the point out of the focal plane does not focus on the confocal pinhole and cannot be detected by the photo-detector, as indicated by a dashed line in Fig. 1a. Thus, a cross sectional image of the object can be obtained at the focal plane with a very shallow focal depth in the order of several

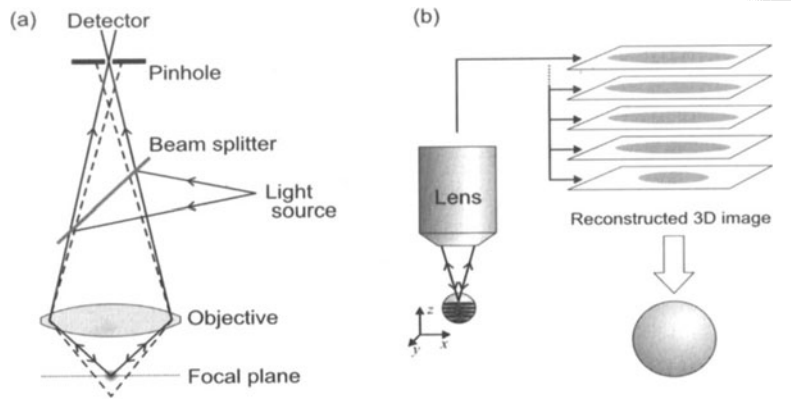

Fig. 1 (**a**) Schematic illustration of a typical optics for confocal microscopy and (**b**) a three-dimensional imaging process. The light from a point source is focused on a tiny point in an object. The signal is collected by the same lens and guided to a detector (*solid path* in *panel a*). The illumination and detection point is scanned point by point to make a microscopy image. The stray light from the point out of the focal plane is rejected by a pinhole put in front of the detector (*dashed line* in *panel a*). Stacking the images at different depths yields a three-dimensional image of the object

hundred nanometers without contribution of surrounding planes. The depth-discrimination with high contrast indicates the ability to observe the object three-dimensionally as shown in Fig. 1b. A set of individual images sliced at different levels affords a three dimensional image over the entire specimen through the reconstruction by image processing on a computer. This is the most striking advantage of confocal microscopy.

In OM, the spatial resolution both lateral (parallel to the focal plane) and axial (perpendicular to the focal plane) is always a critical issue. As to the lateral resolution, laser scanning confocal fluorescence microscopy (LSCFM) has a high resolution of $0.42\lambda/NA$, where NA is the numerical aperture; hence, the use of a large NA objective with blue laser light allows one to achieve a high resolution of less than 200 nm [3]. Polymer films containing coumarine-labeled latex particles with diameters of 500, 220, or 100 nm were examined to estimate the resolution of LSCFM [4]. The measurement of a single latex particle proved that the accuracy of the setup was in the order of 200 nm laterally and 400 nm axially.

2.2 Phase Separation Structures of Polymer Blends

This technique has been successfully applied to investigate phase-separated structures of polymer blends [5, 6]. Li et al. studied surface and bulk morphologies of polystyrene (PS)/poly(methyl methacrylate) (PMMA) blend films and found marked differences in the structure as a function of depth

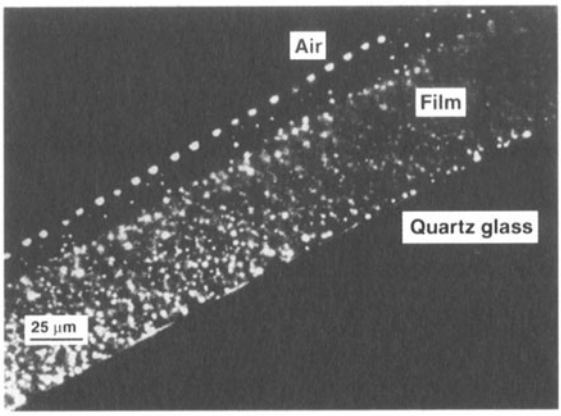

Fig. 2 Cross section morphology of a PS/PMMA blend (9/1) film prepared by casting the solution in toluene at a slow evaporation rate. Bright domains represent the dye-labeled PMMA-rich phase. Reprinted with permission of [7], copyright (1997) American Chemical Society

from the surface [7]. Because interfacial effects are usually dominant for determining the stability of systems particularly in the proximity of the interface, the effects tend to propagate into the bulk and often affect the phase-separation mechanism of the whole film. However, under a slow solvent evaporation rate, the mono-disperse PMMA-rich domains show a highly periodic distribution at the surface. Figure 2 shows a cross-section image of the blend film. There is a depletion layer between the surface and the bulk, in which PMMA molecules are diffusively transferred from the liquid-like bulk to the surface, resulting in a depletion layer free from PMMA-rich particles in between. As this work shows, LSCM provides invaluable information on three-dimensional morphologies even for wet samples containing a liquid phase.

LSCFM has been extensively employed for investigating various polymer systems such as interpenetrating polymer networks (IPN) and polymer latex films. Harmon *et al.* studied thermo-responsive hydrogel networks composed of a crosslinked poly(N-isopropylacrylamide) and a linear polymer of N-alkylacrylamide, and discussed the relationship between the kinetics of the volume phase transition and the phase separated morphology of the semi-IPN [8]. Winnik and coworkers have published many articles on the coalescence process of polymer latex. For example, using a series of sliced images of LSCFM, they visualized the depth profile from the top surface. Consequently the real images successfully clarified the distribution of particles, the size of each domain, and the morphology of blend films in the course of coalescence or segregation of the component polymers [9–11].

2.3 Time Dependent Observation

Another advantage of LSCM and LSCFM is that time evolution of structural changes can be followed. If the temperature of a binary polymer blend is suddenly shifted from the single-phase region to the spinodal region of the phase diagram, the system becomes thermodynamically unstable and starts separating into two phases. This demixing process is well known as spinodal decomposition (SD). The SD process proceeds in the order of 1) early stage, 2) intermediate stage, and 3) late stage. The blend shows a bicontinuous sponge-like structure during the whole stages, while keeping continuous growing of the phase separated structure. The time evolution at each stage has been extensively studied by both scattering methods and microscopic measurements, the latter mostly performed using electron microscopy and LSCFM. Although the structure in the early stage is too small to be visible on LSCFM, the morphology in the intermediate and late stages can be clearly observed in a wide range of dimensions from sub-microns to a millimeter scale at the maximum [12]. For example, Jinnai and coworkers reported a detailed analysis for the time evolution of bicontinuous interface of a phase separated polymer blend in the late stage of SD, using a binary mixture of deuterated polybutadiene (DPB) and polybutadiene (PB) [13, 14]. The latter polymer was labeled with anthracene chromophores in order to obtain a contrast enhancement in fluorescence microscopy. Figure 3 depicts typical LSCFM images showing the growing structure of the phase separated DPB/PB mixture with the elapse of time. Only the PB-rich phase is visible owing to the selective la-

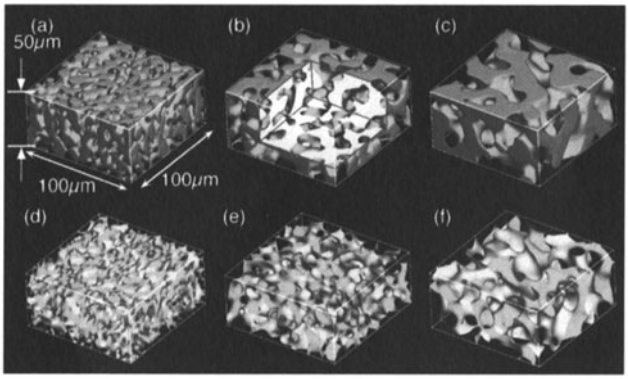

Fig. 3 Time evolution of bicontinuous structures in the DPB/PB blend at the critical composition. The LSCFM images were taken at (**a**) 1675, (**b**) 2880, and (**c**) 4860 min after the onset of SD. These images show only the PB-rich phase labeled with anthracene. Parts (**d**) to (**f**) represent the interface between two coexisting phases for the 3D volume corresponding to (**a**) to (**c**) , respectively. Reprinted with permission of [13], copyright (2000) American Chemical Society

beling with anthracene. On the other hand, the DPB-rich phase is shown as a dark or empty part. From these three-dimensional images, the local curvatures of the interfaces were quantitatively analyzed as a function of time, and it was confirmed that the phase separation process of this mixture well agreed with the prediction of theoretical equations.

Numerous articles have been published over the last decade with emphasis on the time evolution of the SD in binary polymer blends [15–18]. The dynamics could be clarified based on the visual images in three dimensions, owing to the technical development of LSCM and LSCFM.

2.4 Contrast

As shown in the previous figures, labeling is one of important keys for taking excellent images by OM. One needs considerable support of synthetic chemistry to introduce fluorescent probes selectively at a desired position of a polymer chain or to one component of polymer blends. Since each probe has its intrinsic excitation and emission wavelengths, one can get a high sensitivity and contrast in comparison to the non-labeled portion by choosing an appropriate set of the excitation laser light and the detection optical filters. This means that the use of different wavelength light for a given sample allows one to depict selectively one of the components in a multi-colored image, depending on the mechanism of contrast, the source of the signal, and the kind of chemicals etc. For example, an Ar laser (364, 458, 488, and 514 nm) and a He-Ne laser (543 and 633 nm) are often used as convenient light sources supplying various wavelengths. Figure 4 shows again a phase separated morphology of poly(styrene-*ran*-butadiene) (SBR) and polybutadiene (PB) blends [18]. These images were taken by irradiating the sample with two different wavelength light at 488 nm for panel a and 364 nm for the

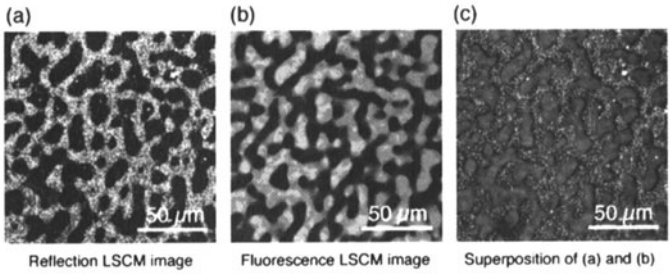

Fig. 4 LSCM images at a depth of 20 μm from the surface of the phase-separated SBR/PB (50/50) blend film. (**a**) Reflection LSCM image observed with $\lambda = 488$ nm (**b**) LSCFM image of the same field as in image (**a**) observed using $\lambda = 364$ nm (**c**) Superposition of the two images, (**a**) and (**b**) PB was labeled with anthracene. Reprinted with permission of [18], copyright (2001) American Chemical Society

middle panel b. Only the latter 364 nm light excited the anthracene labels attached to PB. Hence, the bright part of the middle image indicates the PB-rich domain. At 488 nm, both SBR- and PB-rich domains should be transparent. However, panel a of Fig. 4, which was taken in the reflection mode of LSCM at 488 nm, shows a bicontinuous phase separated structure with a sufficient contrast. These two images are complementary to each other, providing a perfectly superposed image as shown in panel c of Fig. 4. Therefore, the bright area of panel a must be assigned to the SBR-rich domain. This result suggests that the SBR-rich domain has inhomogeneous refractive index with a scale of the wavelength, resulting in a higher reflectivity to the laser light compared to the PB-rich phase. Thus, in addition to the selection of fluorescent probes, LSCM possesses tunability in choosing the wavelength of light to fit with optical properties of the objectives that we intend to see the interior.

2.5 Observation of a Single Polymer

The spatial resolution of LSCFM is still limited to a sub-micron scale. However, it is accessible to a specified volume on the image, in which a small objective can be subjected to fluorescence spectroscopy by means of the optical systems with the intense excitation laser and a highly sensitive light detection apparatus. The fluorescence spectra, time-resolved decay curves, fluorescence polarization, can be observed at a focal point under a microscope. Even in a liquid solution, in which all the solutes rapidly diffuse by Brownian motion, nano-particles of polymer latex and micelles of block copolymers in D_2O are optically trapped, and then their individual fluorescence characteristics can be measured one by one [4]. Since the diameter of a single latex bead or the size of a single micelle is far smaller than the spatial resolution of the microscope, it appears as a tiny bright spot like a star in the picture. It is impossible to see the shape of the particle. However, if the particle is isolated from the others at a sufficiently diluted concentration, LSCFM becomes a powerful tool for spectroscopic studies on a single particle, a single polymer chain, a single molecule etc.

Single molecule fluorescence spectroscopy by LSCFM has often been applied to conjugated polymer molecules, because much attention has been paid to their electro- and photo-functions that is used in light-emitting diodes and other applications such as thin film transistors, sensors, displays, and non-linear optics. Besides these applications, conjugated polymers are suited for LSCFM from a technical point of view, because the large fluorescence intensity from a single chain composed of multiple chromophores allows one to investigate the particular photochemistry and photophysics of the single chain. Poly(p-phenylenevinylene) (PPV) and its derivatives (Scheme 1) have been extensively studied so far [19–25]. A spin-cast film of polystyrene containing extremely diluted PPV-type polymers exhibits small spots

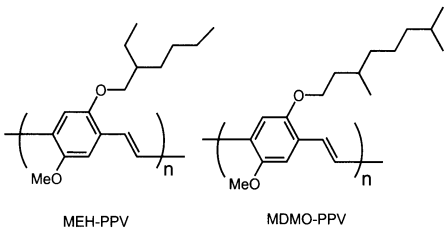

Scheme 1 Chemical structures of Poly(*p* -phenylenevinylene) (PPV) derivatives

of ca. 300 nm in diameter, which are resulted from fluorescence of individual polymer molecules, but blurred by the diffraction limit of light. These spots were assigned to single chains because the density, the number of spots per unit area, varied linearly with the concentration of PPV in the spin-cast solution.

Surprisingly, each spot showed discrete jumps of fluorescence intensity in the transient measurement; the intensity was intermittent and switched rapidly "on" and "off" states as shown in Fig. 5a. This behavior is often found in single molecule spectroscopy due to photobleaching of the chromophore

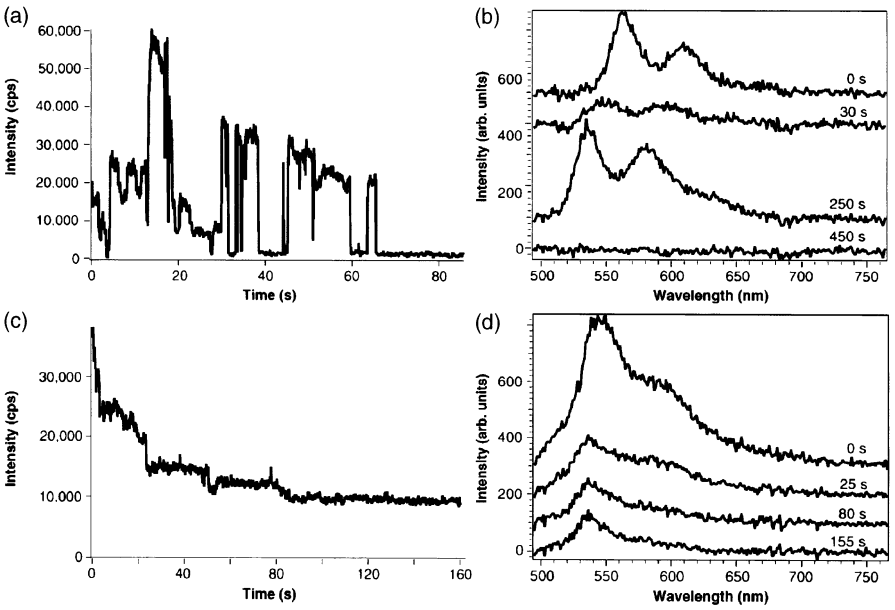

Fig. 5 (**a**), (**c**) Fluorescence intensity transients of a single conjugated polymer (MEH-PPV) spun from toluene and chloroform solution, respectively. (**b**), (**d**) Time-evolution of spectra of a MEH-PPV molecule spun from toluene and chloroform, respectively. Spectra are offset in vertical direction and labeled with the time at which they were taken. Reprinted with permission of [20], copyright (2001) Elsevier

or temporary conversion to a long-lived transient species like a triplet state. However, since the polymer has many chromophores in the chain, it is very hard to understand such a stepwise alteration. To explain this discrete jump, we need to assume that all of the chromophores in the single polymer behave like one molecule. Energy migration along the polymer chain has been suggested to be sufficiently rapid within the lifetime of the excited state (ca. 200 ps), and the excitation energy to collide efficiently with a quenching site produced in the polymer chain. This site could be generated with a photochemical process. For example, photoinduced charge separation occurs easily between an electron-donating chromophore and an acceptor molecule, and the radical cations and radical anions thus produced are known to be efficient quenchers for the excited state of chromophores. A pair of separated charges is a temporary species, which can return to the original state with the charge recombination process. Consequently, the spot intensity of fluorescence reverts back to the initial level.

In addition to this temporary quenching, a permanent defect may be produced by photochemical reactions such as photodecomposition, photooxidation, and photo-isomerization. Once the reaction occurs somewhere in a polymer chain, the bright spot will immediately disappear irreversibly from the image. Fluorescence spectra of the single spot can be measured by LSCFM equipped with an imaging monochromator and a liquid nitrogen cooled CCD [20, 21]. Figure 5b shows time-evolution of fluorescence spectra of a PPV-type molecule adsorbed on a cover glass. At the beginning, the first vibronic band appears around 570 nm, but the spectra shift to the blue side up to 50 nm during continuous excitation at 488 nm. This behavior indicates dispersion of the excitation energy levels in the polymer chain probably due to the local conformation of polymer segments. Energy migration takes place from the high energy level chromophores to the low level sites. Since the lowest site occupies the excitation energy longer than the high level site, it will be first subjected to photoreactions that yield photochemical defects. After consumption of all chromophores at the low levels, the remaining high-energy sites start emitting the fluorescence. Thus the spectral shift indicates temporal changes of the excited state of a single polymer, showing efficient communication among multiple chromophores through rapid energy transfer along the chain.

The discrete behavior of PPV polymers depends on the conformation of polymer chain. If the polymer sample was prepared from a good solvent, or if PPV was embedded in a matrix of low molecular weight PS, the fluorescence intensity transient revealed quite different characteristics from those previously mentioned. The spot showed a gradual decrease in intensity without discrete jumps to the dark level. The fluorescence spectra also gradually decreased in intensity while keeping the peak positions and the vibronic bands as shown in Fig. 5d. These results are usually expected for a multi-chromophoric system, in which the individual chromophores are in-

dependent of each other, and being gradually eliminated one by one from the system by the photobleaching reaction. The different fluorescence behavior is attributed to the difference of conformation of the single polymer chain. When a chain takes an extended conformation, the interaction between adjacent chromophores becomes weak, and then energy migration along the chain is prohibited. Consequently, the polymer emits fluorescence from the multiple chromophores. Thus, the transient and spectroscopic studies by using LSCFM can provide significant insight into the fundamental photophysics occurring in each one of single polymer molecules.

2.6 Single Molecule Spectroscopy

The fluorescence spectrum and its temporal profile provide us extensive information not only on the dye molecule itself but also on the local environment of the surroundings, such as molecular conformation, orientation, and local polarity around the molecule. Therefore, fluorescent dyes have been widely used to probe the local information in the system: various properties of the system is evaluated through the analysis of the fluorescence behavior of the dye molecules introduced [26]. In the conventional fluorescence probe methods, the observed fluorescence was the ensemble average over the numerous molecules which probably show different properties depending on their individual circumstances, histories, and locations. Single molecule spectroscopy allows us to evaluate various characteristics such as distribution, correlation, and time trajectories of the objectives, which are hidden through the process of ensemble averaging. In the single molecule experiment, however, we encounter the difficulty in the signal detection because the fluorescence from a single molecule is extremely weak. Therefore, the highest signal detection efficiency is an absolute requirement for the apparatus. Recent developments in optics with high throughput and sensitivity allow one to perform spectroscopic measurements for a single fluorescent molecule with a large absorption coefficient, a high emission quantum yield, and also high photo-stability such as rhodamine and carbocyanine dyes [27–32]. The single molecule fluorescence probe method has usually been used for dyes dispersed at an extremely low concentration, in order to observe individually molecules by confocal microscopy with a resolution of the diffraction limit. Vallee et al. studied the segmental dynamics of polymers in a glass state through the emission behavior of single 1,1′-octadecyl-3,3,3′,3′-tetramethlindodicarbocyanine (DiD) molecules [28, 30, 31], which were dispersed in a polymer film at a concentration of $< 10^{-9}$ mol L^{-1}. Figure 6a shows the fluorescence image of single DiD molecules, indicating the random orientation of the transition dipole. The fluorescence decay profile for each molecule was observed by a time correlated single photon counting technique. The molecules had different decay rates, indicating the hetero-

geneity of the polymeric glass. In addition to the spatial inhomogeneity, the fluorescence lifetime was temporally heterogeneous, that is, the lifetime fluctuated in time for a given dye molecule. Figure 6b depicts the fluorescence decay curves for the same molecule at different times. As shown in panel c, the fluorescence lifetime varied in time, whereas the fluorescence intensity was almost constant. The fluorescence lifetime of the DiD dye is insusceptible to the molecular conformation and is mainly dependent on the local dielectric constant of the polymeric matrix surrounding the probe molecule [29]. The local polarity at the location of the fluorophore varied in time due to the fluctuation of the free volume generated by segmental motions of the matrix polymer, resulting in the fluctuation of the fluorescence lifetime. The length scale of the cooperative motions responsible for the variation of fluorescence lifetime was evaluated by the theory of Simha and Somcynsky, and the effect of the polymer film thickness on the segmental dynamics was examined. The scale of the cooperative segmental motion decreased with the decrease of the film thickness in the range of < 50 nm, whereas it was constant for the polymer matrix thicker than 50 nm as shown in Fig. 7. This result indicates that the segmental dynamics become faster near the surface. Single molecule spectroscopy is a powerful tool for probing dynamics of polymers because it reveals the various molecular level characteristics hidden in the conventional ensemble averaged measurements. It has a large potential for obtaining insight into the polymer structure and dynamics in a nanometric scale.

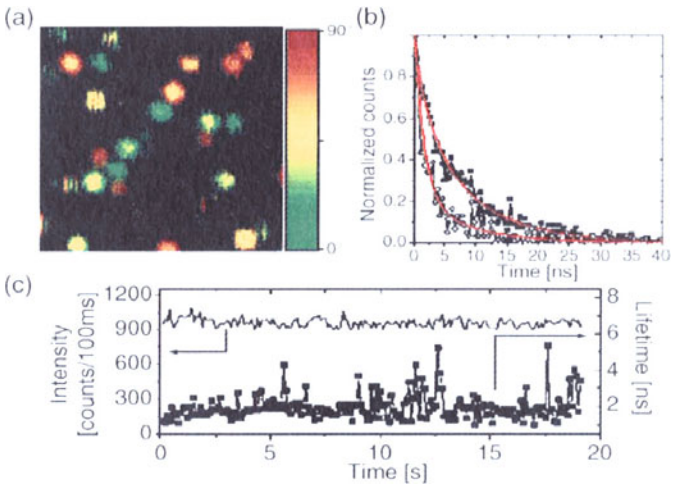

Fig. 6 (**a**) Fluorescence image of single DiD molecules embedded in a polystyrene film ($5 \times 5\ \mu m^2$). The pseudo color scale shows the polarization direction of the fluorescence, indicating the molecular orientation (**b**) Fluorescence decay curves for one DiD molecule at different times. The red lines are the single-exponential functions fitted to the data (**c**) Time traces of fluorescence intensity and lifetime with 100 ms time interval. Reprinted with permission of [30], copyright (2004) American Chemical Society

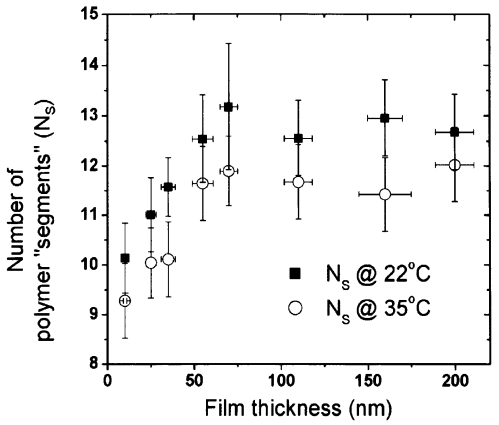

Fig. 7 Film thickness dependence of the number of segments, N_s, involved in the rearrangement volume evaluated by the Simha-Smocynski equation of state. Reprinted with permission of [30], copyright (2004) American Chemical Society

2.7 Recent Advances in Optical Microscopy

The theoretical limitation of the spatial resolution of optical microscopy is defined as the size of the smallest focus area of light. This limitation is called the diffraction limit, which predicts that the spatial resolution of optical microscopy is limited to $\sim \lambda/2$ [33]. The above criterion is based on the assumption that the signal intensity from the object is proportional to the incident power. When the interaction between light and the object is non-linear, this is not the case. The dashed line in Fig. 8 depicts the intensity profile of a diffraction-limited spot. When the object emits signals proportional to the square of the input light intensity, the intensity profile is given by the solid line in Fig. 8. This indicates that the width of the main peak and the intensity of the side-robes decrease for the case of quadratic interaction. Thus, the area emitting the signal light can be reduced by the non-linear optical interaction

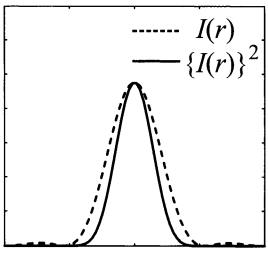

Fig. 8 Radial profiles of linear and quadratic intensity of a diffraction-limited spot, which are indicated by the *dashed* and *solid lines*, respectively

such as harmonic generation and multi-photon absorption, resulting in the improvement of the spatial resolution.

Two-photon excitation fluorescence can be used to improve the resolution of optical microscopy [34–36]. A fluorescent molecule is generally excited from the S_0 state to the S_1 state by absorbing a photon with the energy corresponding to the $S_1 - S_0$ level difference, $\Delta E = h\nu$. In a high photon flux density, the fluorophore can absorb two photons simultaneously. In a two-photon absorption process, the transition probability is proportional to the square of the photon density, resulting in the reduction of the excited area. Simultaneous absorption of two photons by a fluorophore requires the illumination by temporally and spatially confined light with the photon flux density in the order of 10^{30} photons cm^{-1} s^{-1}, which can be obtained by tightly focusing a femtosecond pulse from a mode-locked laser. The fluorescent molecule absorbs two photons at a frequency of $\nu/2$ and is excited to the S_1 state. Therefore, the fluorophore with an absorption band in an ultraviolet-visible range (400–500 nm) can be excited by near-infrared light at a wavelength of 800 to 1000 nm. The infrared excitation beam can penetrate deep into a thick medium without scattering because the scattering efficiency of light is proportional to λ^{-4}. This feature has an important role especially in three-dimensional imaging, which distinguishes the two-photon fluorescence microscopy from other techniques.

Another approach to higher spatial resolution in confocal microscopy is the stimulated emission depletion (STED) scheme [37–40]. The STED technique uses two light sources at different wavelengths. All fluorescent molecules are excited in the diffraction-limited excitation spot of the first source at λ_{ex}, and another beam at a longer wavelength λ_{STED} illuminates the outer part of the excitation focal spot to quench the fluorophore therein. The sequence of the pulses to excitation and depletion with appropriate shapes shrinks the point spread function of the microscope. Figure 9 shows the mechanism of STED. The fluorophore is instantaneously excited to an S_1 state by a first short laser pulse. Immediately after the excitation, the second STED pulse (as long as the fluorescence lifetime) is incident to the excited fluorophore. The STED pulse induces the stimulated emission from the lowest S_1 state to a high vibrational state of S_0 as shown in the Jablonski diagram of Fig. 9a, and the spontaneous emission other than λ_{STED} is detected from the area unirradiated by the STED beam. An appropriate shaping of the STED beam quenches the fluorescence at the outer part of the first excitation spot, and the fluorescence in a gray-scaled range in Fig. 9a is detected only from the very center of the first spot as shown in panel b. Figure 10 shows the fluorescence image of single molecules of rhodamine derivative observed by confocal and STED configurations. In the confocal microscopy image, the single molecules were observed as circular spots with a diameter of 234 nm. On the other hand, the STED microscopy can observe a single molecule in a $\sim$ 140-nm circular shape and clearly distinguish the two molecules sepa-

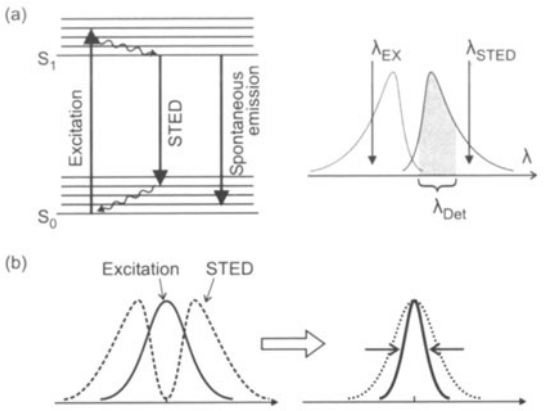

Fig. 9 Schematic illustration of STED. (**a**) Jablonski diagram indicating the S_0 and S_1 state of a molecule (*left*). A femtosecond pulse excites the fluorophore from S_0 to a high vibrational level in S_1. The following slow STED pulse induces the stimulated emission from the lowest S_1 level to a high vibrational level in S_0. The STED pulse depletes the S_1 state and quenches the fluorescence. The corresponding wavelength diagram is shown on the right-hand side: the *dotted* and *solid lines* are the absorption and emission spectra, respectively. The spontaneous emission at λ_{Det} is detected as the signal in the microscopy measurement. (**b**) The combination of the diffraction-limited excitation spot and the engineered STED pulse yields a narrowed point spread function

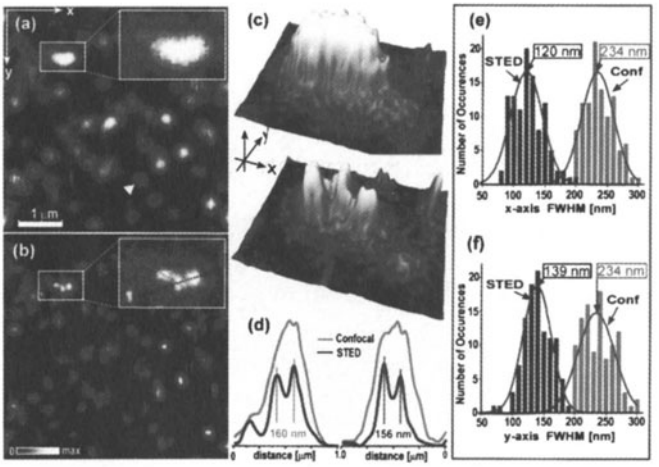

Fig. 10 Fluorescence images of single fluorescent molecules in the same area observed by conventional confocal (**a**) and STED configurations (**b**), and the rectangular areas in both images are enlarged (**c**). Panel d indicates the cross-section profiles for panel (**c**). The STED microscopy clearly resolves the three molecules separated by ~ 160 nm, which were observed as one ellipsoidal spot by the confocal setup. The histograms of the full width at half maximum (FWHM) of the observed fluorescence spots for the *x*- (**e**) and *y*-directions (**f**) indicate the sharpening of the focal spot in the STED configuration. Reprinted with permission of [40], copyright (2003) American Institute of Physics

rated by 160 nm, indicating the high spatial resolution of $\lambda/5$. By the further optimization of the optics and the combination with other techniques such as two-photon fluorescence, the STED microscopy has potential for the super-resolution microscopy in three dimensions and with high detection sensitivity down to the single molecule level. It would be a powerful tool for the structural analysis of biological and polymer materials.

The strategy to achieve a high resolution described above is based on the diffraction-limited optics. The optical microscopy in the next generation utilizes the non-propagating "light". An example of the spatially confined light is the evanescent field generated in a total internal reflection condition. In Fig. 11a, the incident light from the medium 1 with a refractive index n_1 penetrates into the medium 2 with a refractive index n_2, where $n_1 > n_2$. At the interface, total internal reflection occurs at the incident angle θ, given that the angle θ satisfies the condition, $\sin\theta > n_2/n_1$. Under this condition, the incident light slightly penetrates across the interface and reflected. The penetrated light has an imaginary component of the wavenumber vector in the direction normal to the interface, that is, the light cannot propagates in the z-direction but is confined at the interface within a distance of ~ 100 nm, which is called the evanescent light. Total internal reflection (TIR) microscopy illuminates a sample by the evanescent light generated at the sub-

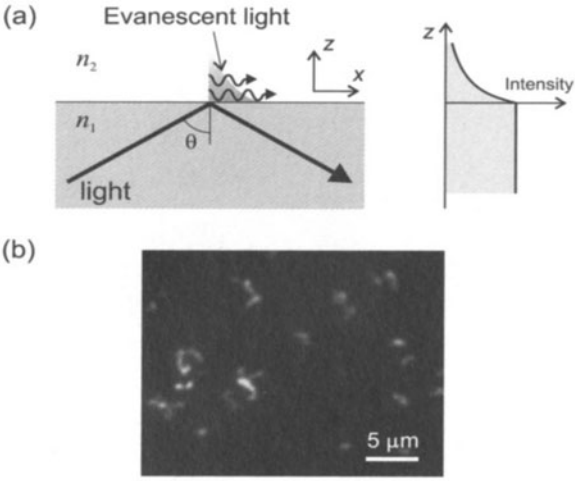

Fig. 11 Schematic drawing of the evanescent field generated in a total internal reflection condition (**a**). When the light is incident from a medium 1 with a high refractive index n_1 to a medium 2 with lower refractive index n_2, total internal reflection occurs in a condition of $\sin\theta > n_2/n_1$. In this situation, the incident light slightly penetrates to medium 2 across the interface, and the penetrating light is called the evanescent light. The evanescent wave propagates in the x-direction and decays rapidly in the z-direction as shown in the intensity profile in the right-hand side. The evanescent light is able to selectively illuminate the specimen at the interface; for example, single DNA molecules adsorbed on a cationic substrate (**b**)

strate surface, and the emission from the specimen was imaged by usual microscopy optics; therefore, the spatial resolution is diffraction-limited in the lateral dimensions. On the other hand, the height resolution is as high as 100 nm at the interface because of the selective excitation of the fluorophore within the region where the evanescent field is confined. The total internal reflection microscopy is suitable for studying dynamic processes at an interface such as the adsorption of single DNA chains onto a solid substrate [41, 42]. Figure 11b presents an example of a TIR microscope image for DNA at a solid/liquid interface.

In total internal reflection microscopy, the light is confined only to the *z*-direction, resulting in the diffraction-limited resolution in the *xy*-plane. In the last two decades a novel optical microscopy has been developed aiming at high spatial resolution by the three-dimensionally localized optical field, "optical near-field". Details on the structural analysis using the near-field microscopy is described in the next section.

3
Nano-Imaging with Near Field Optics

3.1
Outlook of SNOM

Scanning near-field optical microscopy (SNOM) is a new methodology for achieving a high spatial resolution free from the conventional theoretical limitation [43–49]. When the light is incident to a smaller object than its wavelength, there arise not only a propagating field such as scattered light but also a non-propagating electric field restricted around the object, which is called "optical near-field". The non-propagating optical near-field has information on the local structure smaller than the wavelength; therefore, the near-field component can achieve a high spatial resolution beyond the diffraction limit. The basic concept of SNOM was originally suggested more than 70 years ago [50]; however, due to technical difficulties such as the fabrication of a sub-wavelength aperture and the exact position control on a nanometric resolution, it was actually realized only after the invention of scanning probe microscopy in the early 1980's [51, 52]. SNOM is a scanning probe microscopic technique using a probe with a subwavelength-sized aperture. The light incidence to the aperture generates an optical near-field restricted to the vicinity of the probe end as shown schematically in Fig. 12. It allows one to illuminate the specimen and to obtain optical response from the nanometric area, and the raster-scan of the probe builds up the microscopy image with a resolution as high as the aperture size. In many cases, the apertured SNOM probe is fabricated from an optical fiber [46, 47, 53]. The optical fiber

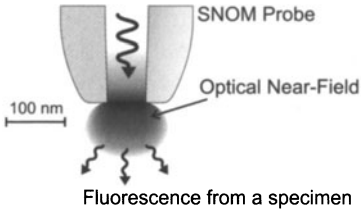

Fig. 12 Schematic illustration of near-field optical microscopy. The optical near-field confined in a nanometric area generates around an aperture much smaller than the wavelength of light

is sharpened mechanically and/or chemically, and the side of the tapered part is metal-coated to leave a small aperture at the sharpened end. As mentioned above, because the near-field intensity rapidly decays with increasing distance from the probe end, the gap between the SNOM probe and the sample surface must be kept constant at a few nanometers while the raster-scanning of the probe. This indicates that SNOM can obtain a topographic image of the sample simultaneously with the optical image. The block diagram of the SNOM system is shown in Fig. 13. The illumination light is coupled to the cleaved end of the fiber probe and guided to the aperture to generate the optical near-field at the sharpened end. The probe end is set above the sample by a force feed-back mechanism similar to AFM. The signal from the specimen is collected by an objective lens behind the substrate, and its intensity is measured by various photo-detectors as a function of the probe position. SNOM has attracted the attention of researchers in many fields of physics, biology, and material science, because it enables one to observe optical properties by spectroscopy in a time-resolved manner, and make polarization measurements

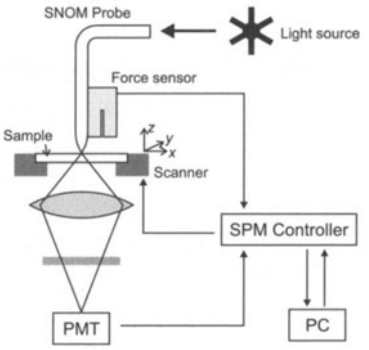

Fig. 13 Block diagram of a SNOM apparatus. The SNOM probe is attached to a piezoelectrics and the force interaction with the sample surface as the measure of the probe-sample distance. The signal light is collected by an objective lens and detected by a photo-multiplier (PMT) through filters or a spectrograph

of single molecule with high sensitivity. The combination of SNOM and the fluorescence method provides the detailed information of the structure and dynamics of the polymer systems with a nanometric spatial resolution.

3.2 Imaging of a Single Polymer Chain

There are many basic and important issues on the morphology of a single polymer chain. Conformation, orientation, end-to-end distance, radius of gyration, elastic modulus, and mobility, all characteristics of a single polymer chain are always fascinating research objects in polymer science. Therefore, many studies aiming at direct imaging of a single polymer chain have been preformed so far to discuss the relationship between the chain morphology and physical properties of polymers. There are various sophisticated works on DNA imaging by means of OM, because a DNA chain is easily visualized by conventional microscope and LSCM owing to the huge molecular weight and the very long chain length over 10 μm. In addition, OM is superior to other types of high-resolution microscopies such as TEM and SEM, since the observation at ambient and biologically relevant conditions is crucial for studying bio-macromolecules like DNA. SNOM has also been used for imaging DNA chains, which are embedded in a lipid membrane, cultured in cells, and adsorbed on a mica surface [54]. Figure 14a shows an example of high-resolution images of a double stranded DNA chain deposited on mica, taken by shear-force topography imaging with a SNOM apparatus. In this figure, the DNA was clearly resolved with a height difference of 1.4 nm, which corresponds to the diameter of the DNA strand. On the other hand, the lateral resolution of this figure was evaluated to be 14 nm from the FWHM of the line profile across the DNA chain. Panel b in Fig. 14 shows a fluorescence image with near-field excitation of a rhodamine-6G (R6G) molecule, which

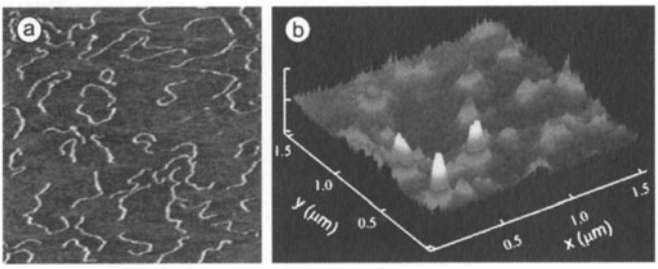

Fig. 14 Shear force image (**a**) and near-field fluorescence image (**b**) of 1kbp DNA fragments labeled with R6G. The DNA sample consists of one fluorophore per strand, and the emission was accumulated for 10 ms/pixel. The maximum signal is 240 counts/pixel and background is 40 counts/pixel. Reprinted with permission of [54], copyright (1998) IOP Publishing Ltd

was labeled at the end of a DNA. Here, the optical data obtained simultaneously with shear force information enables an easy comparison with the high-resolution topography, indicating that each bright spot presents a single R6G molecule at the chain end. Although the intensity varies one by one due to the different circumstances around R6G, some molecules emit fluorescence with intensities 6 times larger than the background level of the photon counting detector, and the diameter of the individual intensity peaks was ca. 70 nm This result suggests that SNOM can provide a clear image of a single DNA chain with a sufficient signal-to-noise ratio and a spatial resolution of 70 nm.

Apart from DNA, the high resolution of SNOM makes it possible to show up the conformational features of a synthetic polymer. Many studies by STM and AFM, both scanning probe microscopes, have already revealed the morphology of isolated chains adsorbed on a flat surface like a mica sheet [55, 56]. In contrast to these scanning probe microscopes, SNOM can detect in situ features of polymer chains located inside the polymer film below the sample surface. As reviewed by Richards et al., the decay length of the evanescent near-field inside the sample depends on the wavelength of light, the aperture diameter, and refractive index of the sample [57, 58]. They estimated the length by the Bethe-Bouwkamp formula for a conjugated polymer blend sample [59]. The calculation for 488 nm laser light through an aperture of 100 nm in diameter showed that the near field light from the tip penetrates to about 100 nm below the surface. Using this advantage, one can get a image of a fluorescently labeled single chain dispersed among large number of identical non-labeled chain matrix [60].

Ultrathin films of poly(isobutyl methacrylate) (PiBMA) have been investigated to demonstrate the ability of single polymer imaging, because they form a stable monolayer on the water surface with a thickness of only 1 nm, and sequential deposition of the monolayer provides very flat thin films with a tailor made inner structure [61]. Scheme 2 depicts the chemical structures of sample polymers. Besides the non-labeled PiBMA homopolymer, a labeled PiBMA (PiBMA-Pe) was synthesized by means of copolymerization of isobutyl methacrylate and 3-perylenylmethyl methacrylate. The copolymer

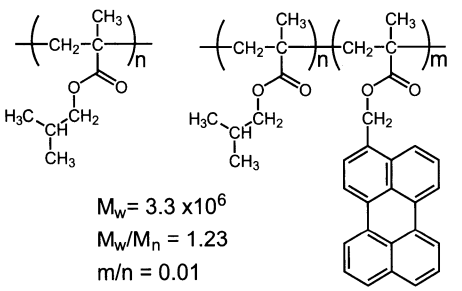

Scheme 2 Chemical structures of PiBMA and perylene labeled PiBMA copolymer

bears perylene (Pe) chromophores at the side chain, whose fraction was suppressed to ca. 1% in order to avoid the influence of labels on the morphology of the polymer chain. In Scheme 2, the molecular weight and its dispersion are also given for labeled PiBMA. The molecular weights of these polymers were very large in the order of 10^6 so that they had large sizes of a few hundred nanometers, hence, their individual features were observable by SNOM with a resolution of 100 nm.

The sample films for SNOM measurements were prepared by the LB technique. Figure 15 shows the layer structure. The PiBMA layer in the middle, in which a very small quantity of PiBMA-Pe was embedded, was sandwiched between the non-labeled layers of poly(vinyl octanal acetal). The near field light from the probe tip excites the Pe dyes attached to the labeled PiBMA-Pe chains that constitute a part of the monolayer film. Thus, the very thin and transparent LB film with a flat surface is regarded as an ideal SNOM sample without any artifacts caused by tip-sample interaction.

Figure 16 shows a SNOM image for PiBMA thin films, containing the labeled PiBMA-Pe polymers with a fraction $F = 0.14\%$, taken with perylene fluorescence intensity under the excitation at 442 nm by a He-Cd laser [26, 60]. Several small spots are observed in the picture, although the surface was very flat over the whole area of the topographic images taken at the same time.

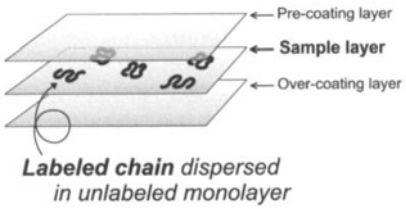

Fig. 15 Layer structure of a sample film containing labeled PiBMA chains in the middle layer of PiBMA. Two monolayers of poly(vinyl octanal acetal) were deposited as the precoat and overcoat layers to protect the specimen from the air and the substrate

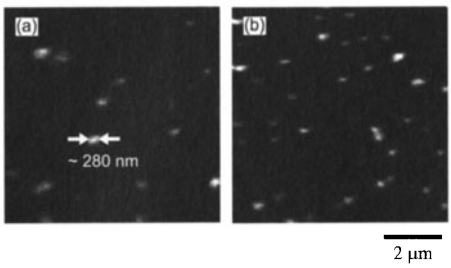

Fig. 16 SNOM images of single polymer chains of PiBMA labeled with perylene, observed by the fluorescence intensity profile. (**a**) $F = 0.14\%$, (**b**) $F = 0.2\%$ The excitation wavelength was 442 nm. Reprinted with permission of [26], copyright (2003) The Chemical Society of Japan

As fraction F was gradually increased, the number of spots also increased. This suggests that each spot corresponds to a single chain incorporated into the monolayer. Another merit of the LB film lies in the well-defined surface area and plane density of molecules. Since the surface area A occupied by a monomer unit of PiBMA is measured by the surface-pressure isotherm, the plane density ϱ of PiBMA-Pe chain is simply given as follows, $\varrho = F/(AD_p)$ where D_p is the degree of polymerization, and then AD_p represents the area occupied by a single PiBMA-Pe chain. The plane density of bright spots in Fig. 16 was in good agreement with the calculated value, indicating that each spot in these pictures represents a single chain embedded in the monolayer. Thus, the quantitative evidence supported the statistically random dispersion of polymer chains in the monolayer.

It is obvious in Fig. 16 that some spots are large and some are small; the spots vary both in size and brightness, probably resulted from molecular weight dispersion of the sample. Although PiBMA has a narrow molecular weight dispersion of $Mw/Mn = 1.23$, there is still a large difference in size from $Mw = 10^6$ to 10^7. However, a large portion of the spots have diameters around 200–300 nm in FWHM of the line profile. Considering the instrumental spatial resolution of ca. 100 nm, the real diameter of a fluorescent polymer is estimated to be ca. 200 nm. This is quite small considering the large molecular weight of the sample polymer. For example, the chain length at a fully extended form is estimated as ca. 8000 nm, on the other hand, the diameter of a circle occupied with a perfectly contracted chain is calculated as ca. 110 nm. Therefore, taking into account these values for a single chain, the SNOM image indicates that the polymers in 2-dimensional monolayers tend to take a contracted conformation as shown in Fig. 17, because they cannot be entangled with other chains and have to exclude each other in order to avoid making free areas in the plane. Although this behavior has been predicted by de Gennes' scaling theory [62], and also by surface viscosity measure-

Fig. 17 Schematic illustration of a single polymer chain contracted in a two-dimensional monolayer. Reprinted with permission of [26], copyright (2003) The Chemical Society of Japan

ments [63, 64], the real image of fluorescence SNOM provided unambiguous evidence of the chain contraction in the two-dimensional polymer systems.

3.3
Phase Separation Structure of Conjugated Polymers

Many of the SNOM studies have been focused on nano-imaging of conjugated polymers. There is great interest in conjugated polymers because of their potential use in a wide variety of electro-optic applications such as thin film transistors, displays, and solar cells. Since the net performance of devices is largely affected by the nano-structure of conjugated polymers, extensive studies have been conducted at a molecular level using TEM and AFM. In contrast to these microscopes, SNOM can provide simultaneously many kinds of images based on a topographic shear force response, optical absorption/fluorescence intensities, and electric response induced by near-field illumination. Hence one can get direct information on the relationships between the nano-structures and the photoinduced electric properties. A typical example of SNOM work is found in the application to light-emitting polymers composed of poly(9,9-dialkylfluorene) (PDF) and its copolymers [57, 58, 65–67]. Figure 18 shows SNOM images of a polymer blend containing 10% poly(9,9-dioctylfluorene-alt-benzothiadiazole) (PDF-B) and 90% another type PDF-based polymer (PDF-P). Panel a in Fig. 18 is a topographic image, where the appearance of protruded domain suggests the phase-separated structure of this blend film. By measuring both the shear force height image (panel a) and fluorescence image (panel b), it becomes possible to distinguish the distribution of PDF-B polymers. Figure 18b was taken with an excitation wavelength at 488 nm, in which only PDF-B was selectively excited, and imaged by collecting the fluorescence through an appropriate filter for PDF-B emission bands. Therefore, the intensity mapping in panel b displays selectively the presence of PDF-B. From these images, the PDF-B domain was unambiguously identified to the protruded

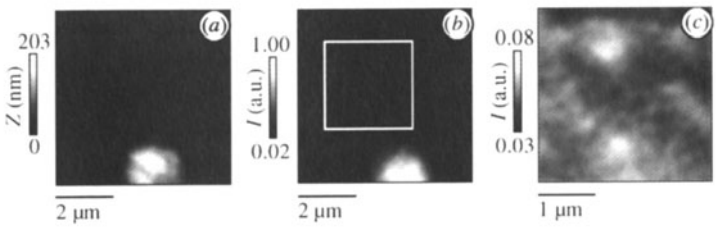

Fig. 18 (**a**) Shear force topographic image of a conjugated PDF blend film with PDF-B/PDF-P= 10/90 (**b**) Corresponding fluorescence SNOM image for (**a**). (**c**) An enlarged fluorescence image taken from the white box shown in (**b**). Reprinted with permission of [58], copyright (2003) The Royal Society

area in the previous topographic image. Figure 18c is an enlarged fluorescence image taken from the dark area of panel b, which is indicated with a white box shown in b and assigned to the PDF-B-poor domain. The magnification in both the *xy*-scales and the intensity signals clearly showed that the PDF-B polymers distributed even in the dark region in panel b, suggesting the presence of further phase separation in a smaller scale far below the spatial resolution of SNOM.

Since PDF is a conjugated and stiff-chain polymer, it tends to afford highly oriented domain structures like liquid crystalline polymers. The alignment of polymer chains results in anisotropic fluorescence, which is polarized parallel to the direction of the stiff backbone. A SNOM image is usually formed by collecting the total intensity of fluorescence in a given wavelength range, while scanning the probe tip over the sample surface. If we can use dual detectors equipped with orthogonal polarizers separately, each component of the polarized fluorescence is detected by two detectors, allowing one to calculate the anisotropy of fluorescence, i.e. the degree of ordering at each point of the sample film with a resolution of 100 nm. Teetsov et al. modified a commercial aperture-type SNOM apparatus to achieve the dual polarization collection; the diagram of their SNOM instrument is shown in Fig. 19 [68–70]. The

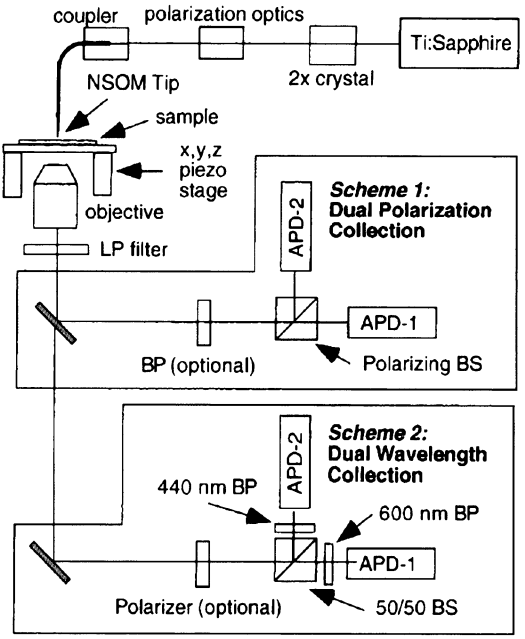

Fig. 19 Diagram of the SNOM instrument equipped with dual detectors for both polarization and wavelength measurements. *Scheme 1*: two images are collected simultaneously at orthogonal polarizations. *Scheme 2*: two images are collected at two wavelengths. Reprinted with permission of [68], copyright (2000) American Chemical Society

fluorescence from a point excited by near-field light from a SNOM tip was collected with a high NA objective, split by a polarizing beam splitter (BS), and then fed onto the dual photon-counting detectors. Consequently, two fluorescence images based on orthogonal polarizations were taken simultaneously. Figure 20 shows SNOM images thus obtained for a pristine PDF film prepared by the spin-coating method. There is almost no contrast in the image of total fluorescence as shown in panel b, which is given by the sum of the signals from the dual detectors. However, both polarization components, indicated by the horizontal and vertical arrows in panels c and d, respectively, provided well-resolved nano-structures of the PDF film. Figure 20e represents the fluorescence anisotropy image calculated by taking subtraction of intensities from the dual detectors (the signals in c and d), and then by dividing it with the total intensity at each pixel. These figures show that the PDF film is composed of the preferentially oriented domain of polymer chains with a size

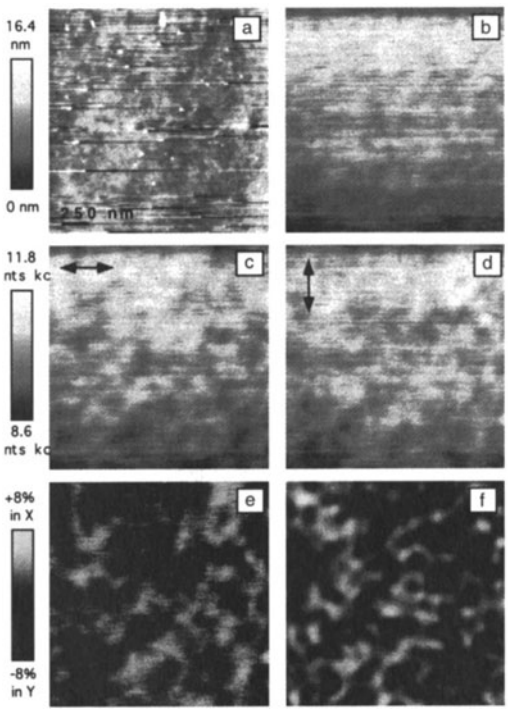

Fig. 20 SNOM images of a 250 nm thick film of poly(9,9-didodecylfluorene) prepared by spin coating from toluene solution: (**a**) topography, (**b**) total fluorescence intensity calculated from sum of the two polarized images (**c**) and (**d**) fluorescence collected simultaneously at orthogonal polarization, (**e**) anisotropy image calculated from panels c and d, and (**f**) simulated anisotropy image assuming the polymers are perfectly oriented in 15 nm cubic domains. Reprinted with permission of [68], copyright (2000) American Chemical Society

of a few tens nanometers. These figures clearly exemplify the feasibility of nano-imaging based on molecular orientation.

Besides PDF derivatives, many SNOM works have been reported using another type of conjugated polymers, poly(phenylene vinylene) (PPV) which is conductive and often used as a hole transporting material in organic devices. The photoinduced electric performances such as excitation energy transfer, charge separation, and charge carrier mobility depend critically on the nano-structures of the polymer assemblies either in pristine bulk films or in blended films with dyes and electron acceptors. Therefore high-resolution SNOM images taken by photo-excitation may provide invaluable information on not only the structures but also the photo-electric performance related to the structure. In addition to the SNOM studies on PDF films, nanometer scale domain structures and phase separated structures of PPV films have been reported by high-resolution imaging of various contrast mechanisms, e.g. transmission [71], fluorescence [72], spectral shifts [73], time-resolving [74], polarization [75], photoconductivity [76], etc. The images were obtained mostly by either the polymer chain alignment or a wavelength shift in the absorption and fluorescence spectra between the order and disorder domains.

3.4
Two-Dimensional Polymer Blends

The morphology of polymer blends in bulk systems has been extensively studied because of the wide range of applications of polymeric materials owing to the improved mechanical and thermal characteristics compared with single component polymers. However, there are few reports on 2-dimensional morphology for polymer blend and its phase-separated structures.

PiBMA is again employed in this section as one component of the monolayer, and poly(octadecyl methacrylate) (PODMA) as another component [77–79]. The former provides a liquid-like monolayer on the water surface, but the latter behaves as a solid-like monolayer due to the strong cohesive force between the long alkyl side chains [80]. Scheme 3 illustrates the chemical structures of the polymers and fluorescent probes. PiBMA and PODMA were labeled separately with pyrene (Py), perylene (Pe), and eosin (Eo) dyes, which were appropriate pairs for energy transfer experiments as a donor and an acceptor. The mixed solution of PiBMA and PODMA was spread on water at 20 °C and then annealed at 40 °C. Figure 21 shows some photos of the phase separation morphology on water during the annealing period, taken by the Brewster Angle Microscope (BAM), indicating the progress of phase-separation on the water surface. The crystalline side chain of PODMA starts melting on water at 40 °C, and the monolayer becomes

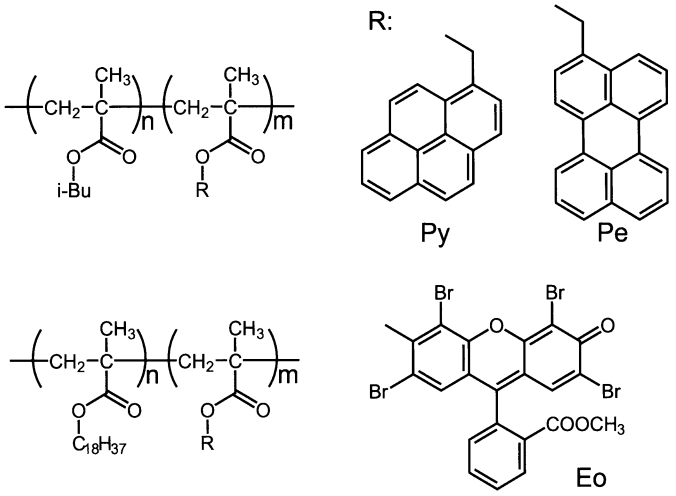

Scheme 3 Chemical structures of PiBMA and PODMA used for two-dimensional phase separation experiments, and the fluorescent labels

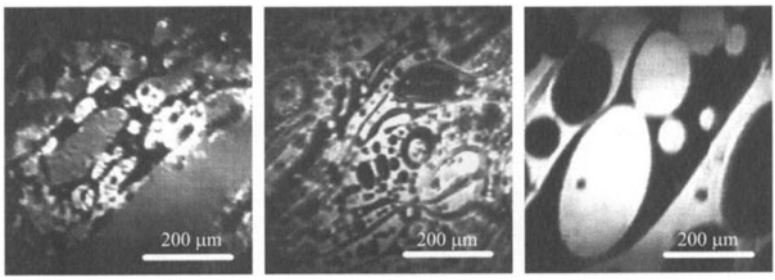

Fig. 21 BAM images of a PiBMA/PODMA mixed monolayer on the water surface at 40 °C. The annealing time was (**a**) 0 min (**b**) 10 min and (**c**) 60 min. Reprinted with permission of [80], copyright (1999) The Society of Polymer Science, Japan

a liquid-like one [80]. Therefore, the phase separation proceeds very quickly, yielding a completely separated monolayer of the polymer blend.

Figure 22 shows three pictures of the PiBMA-Py/PODMA-Pe blend monolayer annealed for 60 min, then deposited on a substrate. These were taken by SNOM with three different filter sets for the excitation and fluorescence wavelengths: panel a is the fluorescence image of Py, which was selectively excited at 325 nm and observed at 370–410 nm; the middle panel b is of Pe fluorescence excited at 442 nm and detected at wavelengths longer than 470 nm [77, 78]. This means that the bright part of panel a indicates the presence of a PiBMA monolayer, and the bright area of panel b corresponds to the PODMA monolayer. These two pictures show perfectly complementary features of two components, indicating that the phase separation was com-

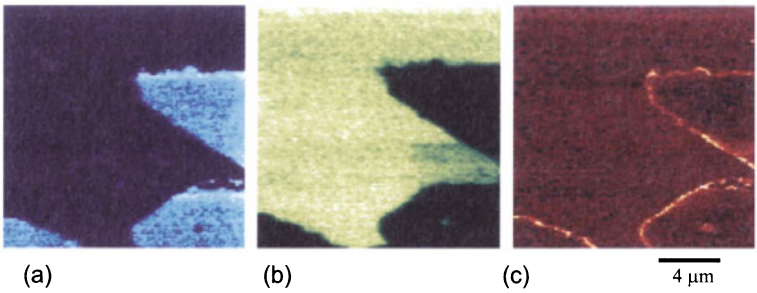

Fig. 22 Fluorescence SNOM images of a phase-separated polymer monolayer after annealing for 60 min. The scanning area was $15 \times 15\ \mu m^2$ and the scale bar indicates 4 μm. (**a**) Py fluorescence image. The excitation wavelength was 325 nm and the optical filters used collected only the fluorescence of Py (**b**) Pe fluorescence image, taken by 442 nm excitation and by emission at wavelengths longer than 470 nm (**c**) Energy transfer image. The excitation wavelength was 325 nm and the Pe fluorescence was collected with the same optical filters as in (**b**). Reprinted with permission of [77], copyright (1999) American Chemical Society

plete, and that the surface was covered by one of them without any cracks or defects.

As shown in panel c in Fig. 22, it is very interesting to take a SNOM image with excitation of Py at 325 nm and by monitoring Pe fluorescence at wavelengths longer than 470 nm. Under these experimental conditions, Py was selectively excited, but Py fluorescence could not be detected. Therefore, the fluorescence from Pe observed was emitted only through the excitation energy transfer from Py to Pe. Hence, the bright area in panel c indicates the boundary region, in which PiBMA-Py/PODMA-Pe were molecularly mixed and two different labels approached each other within the Foerster radius (critical energy transfer radius) of 3.3 nm. Thus, the energy transfer mapping by SNOM provides a novel method to depict the area molecularly mixed at the phase boundary. This technique will be applicable to other molecular assemblies and polymer systems for indicating the degree of mixing at the molecular level.

SNOM is capable of obtaining simultaneous optical and topographic images with a high-resolution. Furthermore, it can be equipped with a time-correlated single photon counting system and a short-pulse laser system in order to obtain images of fluorescence, or to measure fluorescence decays at individual points with a spatial resolution of less than 100 nm. The further utility of energy transfer mapping can be recognized by point-by-point analysis of the fluorescence decay curves under the SNOM image. The samples used in this experiment were PODMA-Pe as the donor and PiBMA-Eo as the acceptor. The Eo dyes of the latter component quench the excited state of the former Pe through the energy transfer mechanism. The closer the mutual distance of these two dyes, the faster the rate constant of quenching is. Therefore,

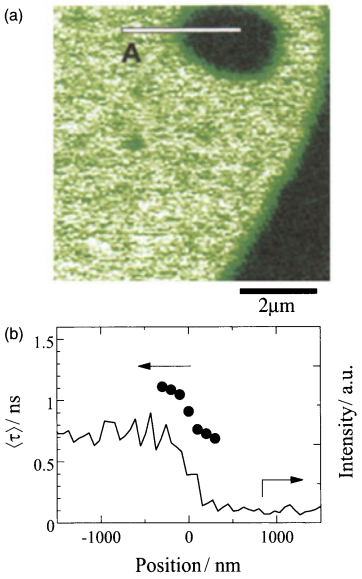

Fig. 23 (**a**) SNOM image for a PODMA-Pe/PiBMA-Eo monolayer after annealing for 60 min (**b**) Fluorescence lifetime and intensity profiles. The excitation wavelength was 415 nm. The *closed circles* and the *solid line* indicate the lifetime and the intensity, respectively, measured along the line A in panel a. Reprinted with permission of [78], copyright (2001) American Chemical Society

the decay rate of Pe fluorescence reflects the local concentration of Eo dyes around Pe molecules at the observed point.

Figure 23b shows the line profiles across the boundary of PODMA-Pe/PiBMA-Eo along the solid line indicated in panel a [78]. In panel b, the fluorescence intensity and lifetime of Pe emission are plotted at every 100 nm displacement over the whole length of the boundary region. As shifting the position observed from the PODMA phase to PiBMA phase, both the fluorescence intensity and the lifetime of Pe decrease steeply, showing a rapid increase of the concentration of Eo dyes attached to PiBMA segments. The intensity of fluorescence is simply proportional to the number of Pe under the aperture of SNOM, which may be changed with morphological distribution of Pe polymers, irrespective of the local concentrations of Pe and Eo. On the other hand, the lifetime measurement directly manifests the alteration of local concentration of Eo chromophores around Pe at the specific point. Therefore, the lifetime profile in Fig. 23 provides unambiguous indication for the gradient of the composition of both polymers across the boundary of two domains. These experiments show the high potential of the energy transfer method for the structural analysis, when it is combined with nanometric time-resolving microscopy.

3.5 Polymer Networks

The three-dimensional network of polymer chains has also attracted much attention in polymer science and technology. Although a great number of researchers have devoted their efforts toward clarifying the network structure using X-ray diffraction, light scattering, and optical microscope measurements, the origin of the unique and particular properties is not yet understood in relation to the structure of networks. The microscopic images of polymer gels in real space have been reported only at low magnifications in a micrometer scale using optical LSCM and LSCFM [18, 81], whereas polymer gels are known to form fractal structures over a wide range of dimensions from nanometer to micrometer regions. A large-scale structure observed is made of microscopic structures in a nanometric scale, that are again composed of molecular scale assemblies with a huge number of polymer chains. Therefore, nano-imaging of polymer gel may provide novel insight into the networks yet invisible so far. Here, we introduce an application of SNOM for a PMMA chemical gel labeled with fluorescence probes such as Pe and Eo chromophores [82].

The sample was prepared by radical copolymerization of MMA monomer in toluene solutions containing a small amount of 3-perylenylmethyl methacrylate as a fluorescent monomer and ethylene glycol dimethacrylate as a cross-linker. The sample for SNOM measurements was prepared from the solid gel thus obtained, which was sliced using a microtome, yielding a very thin film with a thickness of ca. 100 nm, and then the inner structure was observed by SNOM.

Figure 24 shows three pictures taken in different SNOM modes. Panel a is the shear force topographic picture, in which the oblique lines display scratch of the surface made with the knife edge of the microtome. Panel b shows an

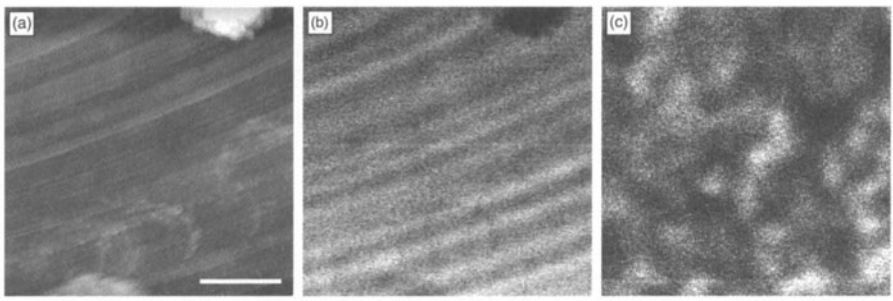

Fig. 24 SNOM images of a polymer network of PMMA with cross link density of 0.1%. (**a**) Shear force topographic image, (**b**) transmission image and (**c**) fluorescence image. The scale bar indicates 1 μm and the wavelength of the light source was 442 nm. Reprinted with permission of [82], copyright (2000) American Chemical Society

optical transmission image obtained by scattered light at the surface. As like as panel a, the surface topography appeared, showing only oblique lines made by the knife edge. However, panel c in Fig. 24, image of fluorescence of Pe in the same area as panels a and b, shows inhomogeneous distribution of fluorescence intensity, instead of the surface topography. The structure with a size of 500–600 nm was observed, suggesting the inhomogeneous and domain-like network structure of the PMMA gel. These pictures indicate that SNOM can be used to reveal the nano-structures inside the sample film, whereas AFM gives simply topographic images of the surface. The size of inhomogeneity became markedly small with the increase in crosslink density. These results indicate that the SNOM picture taken in the fluorescence mode actually represents the fluctuation of segment density in the polymer networks, although the fluorescent probes were introduced into the polymer chains at a statistically random distribution.

The inhomogeneous structure was monitored by the energy transfer method. The rate of energy transfer between a donor molecule and an acceptor molecule is determined by the distance of separation in a nanometer dimension. Therefore, the inhomogeneity of segment density results in faster decay of donor fluorescence compared with homogeneous distribution. To observe this phenomenon, Pe and Eo dyes were introduced into the PMMA

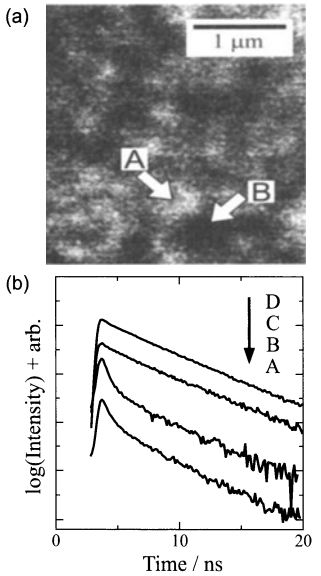

Fig. 25 (**a**) Fluorescence SNOM image of a PMMA gel labeled with Pe and Eo dyes (**b**) Fluorescence decay curves of Pe observed for: (curves A and B) PMMA gel at points A and B indicated in panel a, (curve C) PMMA bulk sample without crosslinker, (curve D) spin-cast PMMA film containing Pe dyes. Reprinted with permission of [26], copyright (2003) The Chemical Society of Japan

chains in the gel; the latter dye Eo acts as an energy acceptor for the Pe donor. Figure 25a shows again a SNOM picture of PMMA gel, in which the marked positions A and B were examined by the time-resolving measurement for Pe fluorescence and the decay data are shown in Fig. 25b. The decay functions at these points obviously consist of multi-component functions, but the average lifetimes are far shorter than the intrinsic decay function of the isolated Pe in a spin-cast film, which is plotted with the line D. For comparison, a control PMMA sample labeled with both Pe and Eo dyes was prepared at the same concentrations as the gel. This spin cast film provides a homogeneous distribution of these dyes in the bulk, hence the decay curve C is very similar to curve D for the isolated Pe with a random distribution. These results indicate that the PMMA gel has large local densities at least 10 times higher than the homogeneous distribution.

It is also very interesting that the fast decay rate due to the high density of polymer segment was almost constant irrespective of the positions observed. As seen in Fig. 25a, point A is much brighter than point B, suggesting that the segment density at A is higher than that at B. However, the energy transfer experiment obviously indicates that the density is independent of the observed position. This discrepancy can be explained by assuming a structural hierarchy of PMMA gel. Since the energy transfer takes place between molecules closer than ca. 10 nm, the fluorescence decay function indicates the local environment of a micro-cluster in the molecular scale of 1–10 nm. In a larger scale of 10–1000 nm, the clusters are connected and form aggregates with an inhomogeneous structure, which was observed by the fluorescence SNOM. Therefore, the dark and bright parts of SNOM image represent simply the small and large numbers of clusters, respectively, in which the local concentration of polymer segment in the molecular level is always very high, regardless of the brightness of the SNOM image in a large scale of a few hundred nanometers.

3.6
Development of SNOM

Previous SNOM measurements have been performed by detecting the fluorescence signal from the specimen in many cases. Fluorescence SNOM is so sensitive that it can detect the signal from a single molecule and provides valuable information such as the orientation and spatial distribution of the fluorescent molecules not only from the intensity but also from the spectra and time-resolved profiles. Needless to say, however, the fluorescence SNOM measurement can be applied only to the chemical species which is fluorescent in a visible range. For a non-fluorescent specimen, the fluorescence labeling must be carried out, but the introduction of dye molecules often involves complicated chemical synthetic processes. The fluorescence SNOM limits its versatility in variation of observable species, while it is

highly sensitive and gives one various kinds of molecular information. Therefore, another spectroscopic method is desired to directly observe a variety of chemicals. Vibrational spectroscopy could be a promising technique for the SNOM measurement with chemical information [83–89]. The infrared absorption and Raman scattering spectra can be obtained for all chemical species in principle, and they provide much information on the chemicals as the "fingerprint" of a molecule. Therefore, the vibrational spectroscopy SNOM has attracted the attention of many researchers because it would allow the direct spectral characterization of various chemicals with a nanometric spatial resolution. However, Raman scattering spectroscopy has been considerably difficult because the Raman scattering cross section is very low (a factor of 10^{14}) compared to that for fluorescence emission. It is well known that the Raman scattering intensity is greatly enhanced on a rough metal surface: surface enhanced Raman spectroscopy (SERS). The SERS mechanism was introduced to excite the specimen in a local area in order to increase the Raman intensity. In Raman SNOM, a sharp metal stylus without an aperture is used; this type of SNOM is often called the apertureless SNOM in contrast to the SNOM using an optical fiber probe. The sample is illuminated by a focused laser beam in a diffraction-limited size. A sharp metal tip (a gold or silver-coated AFM cantilever is typically used) is on the focal spot. At the tip end, the electric field intensity is enhanced by the surface

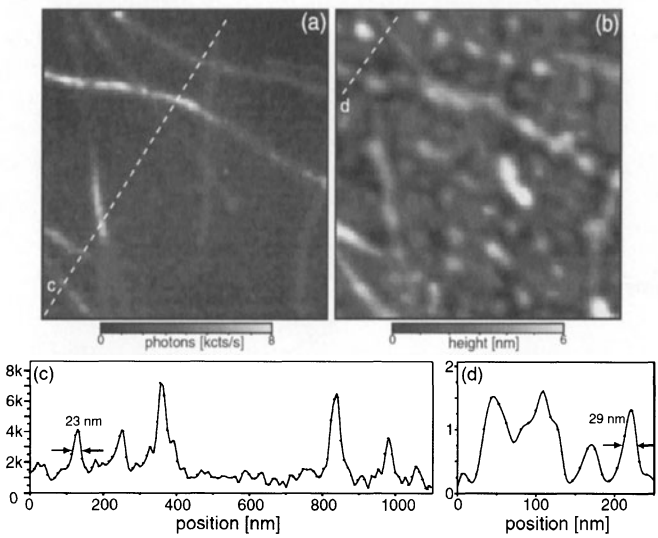

Fig. 26 (**a**) Near-field Raman image and (**b**) simultaneously obtained surface topography of single wall carbon nanotubes. Scan area is $1 \times 1\ \mu m^2$ Numerous circular features in the topography are attributed to contaminant water droplets. The cross-section profiles for Raman and topographic images are shown in panels c and d, respectively. Reprinted with permission of [87], copyright (2003) American Institute of Physics

plasmon excitation of the metal tip. This localized and enhanced field excites the specimen and induces the detectable Raman scattering from a nanometric area [84–87]. Figure 26 indicates the Raman SNOM image of single wall carbon nanotubes (SWNTs), which was obtained by collecting the G′ band of SWNT at a wavenumber of 2615 cm^{-1} attributed to the overtone of the defect mode. In the Raman scattering image of Fig. 26a, the individual SWNTs are clearly imaged, whereas a lot of circular dots are seen besides the SWNTs in the simultaneously observed topographic image of panel b. This indicates the ability of the Raman SNOM to distinguish chemical species. Each SWNT was observed as a strand with a width of 23 nm, indicating the high spatial resolution better than $\lambda/25$. With regard to the infrared spectroscopy, the absorption contrast for the minute sample volume in the order of attoliter. Keilmann and his co-workers have reported that the scattering intensity in the apertureless SNOM configuration is dependent on the infrared absorption at the illumination wavelength [88, 89]. A phase-separated blend of PS and PMMA was observed at wavelengths of 9.68 and 10.17 μm, which were attributed to the absorption bands for PS and PMMA, respectively, and each component was distinguished by selecting the appropriate wavelength

The near-field vibrational spectroscopy has been greatly developed in recent years. However, the number of chemical species practically imaged is

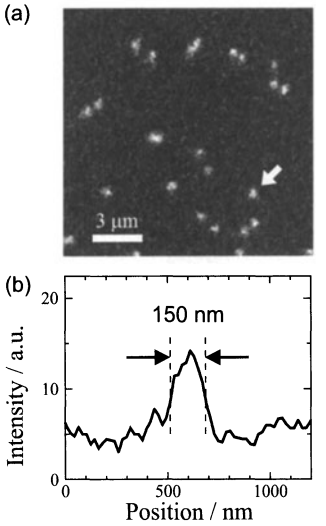

Fig. 27 (**a**) DUV-SNOM image of polystyrene nano-particles with a diameter of 100 nm (**b**) As shown in the cross-section profile for the arrowed particle, the bead has a circular shape with a diameter of 150 nm This indicates the high spatial resolution beyond the diffraction limit. Reprinted with permission of [90], copyright (2004) American Institute of Physics

still limited. In contrast to the vibrational characterization, another approach has been reported for the direct imaging of a variety of chemicals, that is, near-field fluorescence spectroscopy in the deep ultra-violet (DUV) region [90]. The DUV light at a wavelength below 300 nm can induce the π–π^* transition of a carbon-carbon double bond. For example, benzene has an absorption band around 250 nm and emits the fluorescence at 270–300 nm. Therefore, all aromatic chemical species can be excited in the DUV range. Previously, we could not use the UV light shorter than 400 nm in SNOM because it is strongly absorbed by the dopant included in the core of the fiber probe. In the DUV-SNOM, the probe is fabricated from an optical fiber with a pure quartz core, which is transparent at $\lambda > 220$ nm. Figure 27 indicates the DUV-SNOM image of nano-spheres of PS with a diameter of 100 nm. The side-chain phenyl group in PS was excited by the near-field at a wavelength of 266 nm, and the benzene excimer emission at 300–340 nm was collected. The PS beads were clearly observed in the DUV-SNOM image. The observed diameter for the 100 nm beads was ca. 150 nm, indicating the high spatial resolution better than 100 nm beyond the diffraction limit. Thus, DUV-SNOM allows direct imaging of the aromatic polymer without any chemical modification such as fluorescence labeling. Figure 28 shows a DUV-SNOM image for a phase-separated polymer blend composed of PS and PMMA, in which the former PS domains were selectively observed without any fluorescent labels. As mentioned above, also the Raman SNOM would enable the direct

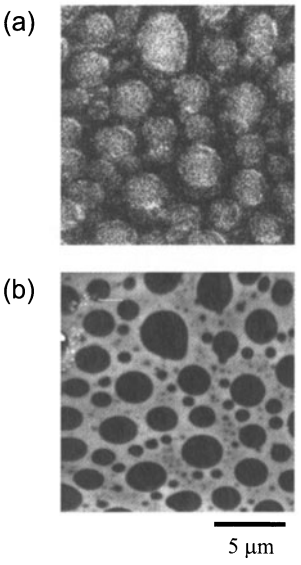

Fig. 28 (**a**) DUV-SNOM and (**b**) topographic images of a phase separation structure of a polystyrene/poly(methyl methaacrylate) blend thin film. The polystyrene is directly observed without any labeling procedure

imaging of chemicals. Due to the difficulty of signal enhancement, however, Raman imaging has been reported for only a few kinds of chemicals at the present stage. On the other hand, since DUV-SNOM is operated by collecting the inherently strong fluorescence emission, a variety of chemicals can be observed with the high sensitivity and the sub-wavelength spatial resolution. The direct imaging by the DUV-SNOM has been performed not only for PS but also other aromatic polymers and biological materials: polycarbonate, poly(ehtyleneterephthalate), proteins, and DNA. Thus, DUV-SNOM expands the range of wavelength and chemicals examined, and provides versatile spectroscopic techniques useful in the analysis of polymer systems.

4 Summary

Optical microscopy, a conventional tool for investigating materials, is still making great progress with the introduction of novel optical techniques. In recent years LSCM has been introduced to a variety of scientific fields, exhibiting the particular advantage of 3-dimensional imaging with a submicron scale resolution, while keeping the merits of an optical method such as high sensitivity of detection, time-resolution for molecular and excitation dynamics and spectroscopic analysis of materials. SNOM has brought further improvement particularly in the spatial resolution beyond the diffraction limit of light, and has extended the ability of optical analysis to nanometer dimensions. With the aid of novel ideas and techniques, SNOM has been continuously improved both in resolution and in sensitivity. It has already realized single molecule detection with a lateral resolution of ca. 30 nm, which is one order higher than the resolution of LSCM and two orders higher than the resolution of conventional optical microscopes. The importance of nanoscale science is now widely recognized, and much attention has been paid to organic materials and their assemblies. Therefore, optical microscopy is expected to make more contributions to the soft materials science as a tool for seeing in nanometer dimensions.

References

1. Wilson T (1990) Confocal Microscopy. Academic Press, London
2. Webb RH (1996) Rep Prog Phys 59:427
3. Brakenhoff GJ, Blom P, Barends P (1979) J Microsc 117:219
4. Gensch T, Hofkens J, van Stam J, Faes H, Creutz S, Tsuda K, Jerome R, Masuhara H, De Schryver FC (1998) J Phys Chem B 102:8440

5. Verhoogt H, van Dam J, Posthuma de Boer A, Draaijer A, Houpt PM (1993) Polymer 34:1325
6. Li L, Sosnowski S, Chaffey CE, Balke ST, Winnik MA (1994) Langmuir 10:2495
7. Kumacheva E, Li L, Winnik MA, Shinozaki DM, Cheng PC (1997) Langmuir 13:2483
8. Harmon ME, Schrof W, Frank CW (2003) Polymer 44:6927
9. Vorobyova O, Winnik MA (2001) J Polym Sci B 39:2317
10. Vorobyova O, Winnik MA (2001) Macromolecules 34:2298
11. Wu J, Li H, Winnik MA, Farwaha R, Rademacher J (2004) J Polym Sci A 42:5005
12. Ribbe AE, Hashimoto T (1997) Macromolecules 30:3999
13. Jinnai H, Nishikawa Y, Morimoto H, Koga T, Hashimoto T (2000) Langmuir 16:4380
14. Jinnai H, Kitagishi H, Hamano K, Nishikawa Y, Takahashi M (2003) Phys Rev E 67:021801
15. Newby BZ, Composto RJ (2000) Macromolecules 33:3274
16. Moffitt M, Rharbi Y, Tong JD, Farhina JPS, Li H, Winnik MA, Zahalka H (2003) J Polym Sci B 41:637
17. Ma Y, Farinha JPS, Winnik MA, Yaneff PV, Ryntz RA (2004) Macromolecules 37:6544
18. Jinnai H, Yoshida H, Kimishima K, Funaki Y, Hirokawa Y, Ribbe AE, Hashimoto H (2001) Macromolecules 34:5186
19. Vanden Bout DA, Yip W-T, Hu D, Fu D-K, Swager TM, Barbara PF (1997) Science 277:1074
20. Huser T, Yan M (2001) J Photochem Photobio A 144:43
21. Huser T, Yan M, Rothberg LJ (2000) Proc Natl Acad Sci USA 97:11187
22. Sartori SS, De Feyter S, Hofkens J, Van der Auweraer M, De Schryver F, Brunner K, Hofstraat JW (2003) Macromolecules 36:500
23. Schindler F, Lupton JM, Feldmann J, Scherf U (2004) Proc Natl Acad Sci USA 101:14695
24. Hu D, Yu J, Barbara PF (1999) J Am Chem Soc 121:6936
25. Lee J, Lee J, Lee M, Lee K-J-B, Ko D-S (2004) Chem Phys Lett 394:49
26. Ito S, Aoki H (2003) Bull Chem Soc Jpn 76:1693
27. Vallee RAL, Cotlet M, Hofkens J, De Schryver F, Muellen K (2003) Macromolecules 36:7752
28. Vallee RAL, Tomczak N, Kuipers L, Vancso GJ, van Hulst NF (2003) Phys Rev Lett 91:038301
29. Vallee RAL, Vancso GJ, van Hulst NF, Calbert JP, Cornil J, Bredas JL (2003) Chem Phys Lett 372:282
30. Tomczak N, Vallee RAL, van Dijk EMH, Kuipers L, van Hulst NF, Vancso GJ (2004) J Am Chem Soc 126:4748
31. Tomczak N, Vallee RAL, van Dijk EMH, Garcia-Parajo M, Kuipers L, van Hulst NF, Vancso GJ (2004) Euro Polym J 40:1001
32. Hofkens J, Vosch T, Maus M, Koehn F, Cotlet M, Weil M, Herrmann A, Muellen K, De Schryver FC (2001) Chem Phys Lett 333:255
33. Born M, Wolf E (1980) Principles of Optics. Pergamon Press, Oxford
34. Denk W, Strickler JH, Webb WW (1990) Science 248:73
35. Diaspro A, Robello M (2000) J Photochem Photobiol B:Biol 55:1
36. Nakamura O (1999) Microsc Res Tech 47:165
37. Hell SW, Wichmann J (1994) Opt Lett, 19:780
38. Klar T, Hell SW (1999) Opt Lett 24:954
39. Klar T, Jakobs S, Dyba M, Egner A, Hell SW (2000) Proc Nat Acad Sci USA 97:8260

40. Westphal V, Blanca CM, Dyba M, Kastrup L, Hell SW (2003) Appl Phys Lett 82:3125
41. Osborne MA, Barnes CL, Balasubramanian S, Klenerman D (2001) J Phys Chem B 105:3120
42. Kang SH, Shortreed MR, Yeung ES (2001) Anal Chem 73:1091
43. Paesler MA, Moyer PJ (1996) Near-Field Optics: Theory, Instrumentation, and Applications. John Wiley & Sons, New York
44. Ohtsu M (1998) Near-Field Nano/Atom Optics and Technology. Springer, Tokyo
45. Kawata S, Ohtsu M, Irie M (2002) Nano-Optics. Springer, Berlin
46. Betzig E, Trautman JK, Harris TD, Weiner JS, Kostelak RL (1991) Science 251:1468
47. Betzig E, Trautman JK (1992) Science 257:189
48. Vanden Bout DA, Kerimo J, Higgins DA, Barbara PF (1997) Acc Chem Res 30:204.
49. Dunn RC (1999) Chem Rev 99:2891
50. Synge EH (1928) Phil Mag 6:356
51. Binnig G, Rohrer H, Gerber Ch, Weibel E (1982) Phys Rev Lett 49:57
52. Binnig E, Quate CF, Gerber Ch (1986) Phys Rev Lett 56:930
53. Pangaribuan T, Yamada K, Jiang S, Ohsawa H, Ohtsu M (2002) Jpn J Appl Phys 31:L1302
54. Garcia-Parajo MF, Veerman JA, van Noort SJT, de Grooth BG, Greve J, van Hulst NF (1998) Bioimaging 6:43
55. Kumaki J, Nishikawa Y, Hashimoto T (1996) J Am Chem Soc 118:3321
56. Kumaki J, Hashimoto T (1998) J Am Chem Soc 120:423
57. Richards D, Cacialli F (2004) Phil. Trans R Soc Lond. A 362:771
58. Richards D (2003) Phil. Trans R Soc Lond. A 361:2843
59. Bethe HA (1944) Phys Rev 66:163
60. Ito S, Aoki H, Anryu M (2001) Trans Mater Res Soc Japan 26:929
61. Naito K (1989) J Colloid Interface Sci 131:218
62. de Gennes PG (1979) Scaling Concepts in Polymer Physics. Cornell University, Ithaca, N.Y.
63. Sato N, Ito S, Yamamoto M (1996) Polym J 28:784
64. Sato N, Ito S, Yamamoto M (1998) Macromolecules 31:2673
65. Stevenson R, Milner, RG, Richards D, Arias AC, Mackenzie JD, Halls JJM, Friend RH, Kang DJ, Blamire M (2001) J Microscopy 202:433. (S22 PF)
66. Chappell J, Lidzey DG (2003) J Microscopy 209:188. (N19 blend PF)
67. Kwak ES, Kang TJ, Vanden Bout DA (2001) Anal Chem 73:3257. (N31 decay)
68. Teetsov J, Vanden Bout DA (2000) J Phys Chem B 104:9378
69. Teetsov J, Vanden Bout DA (2001) Macromol Symp 167:153
70. Teetsov J, Vanden Bout DA (2002) Langmuir 18:897
71. Hsu JH, Wei PK, Fann WS, Chuang KR, Chen SA (1998) Ultramicroscopy 71:263
72. DeAro JA, Lemmer U, Moses D, Buratto SK (1999) Synthetic Metals 101:300
73. Schaller RD, Lee LF, Johnson JC, Haber LH, Saykally RJ, Vieceli J, Benjamin H, Nguyen TQ, Schwartz BJ (2002) J Phys Chem B 106:9496
74. Nabetani Y, Yamasaki M, Miura A, Tamai N (2001) Thin Solid Films 393:329
75. Tan CH, Inigo AR, Hsu JH, Fann W, Wei PK (2001) J Phys Chem Solids 62:1643
76. DeAro JA, Moses D, Buratto SK (1999) Appl Phys Lett 75:3814
77. Aoki H, Sakurai Y, Ito S, Nakagawa T (1999) J Phys Chem B, 103:10553
78. Aoki H, Ito S (2001) J Phys Chem B 105:4558
79. Aoki H, Kunai Y, Ito S, Yamada H, Matsushige K (2002) Appl Surf Sci 188:534
80. Sakurai Y, Sato N, Ito S, Yamamoto M (1999) Kobunshi-Ronbunshu 56:850
81. Hirokawa Y, Jinnai H, Nishikawa Y, Okamoto T, Hashimoto T (1999) Macromolecules 32:7093

82. Aoki H, Tanaka Ito SS, Yamamoto M (2000) Macromolecules 33:9650
83. Jahncke CL, Paesler PA, Hallen HD (1995) Appl Phys Lett 67:2483
84. Deckert V, Zeisel D, Zenobi R, Vo-Dinh T (1998) Anal Chem 70:2646
85. Hayazawa N, Inouye Y, Sekkat Z, Kawata S (2001) Chem Phys Lett 335:369
86. Hayazawa N, Yano T, Watanabe H, Inouyea Y, Kawata S (2003) Chem Phys Lett 376:174
87. Hartschuh A, Sanchez EJ, Xie SX, Novotny L (2003) Phys Rev Lett 90:095503
88. Knoll B, Keilmann F (1999) Nature 399:134
89. Taubner T, Hillenbrand R, Keilmann F (2004) Appl Phys Lett 85:5064
90. Aoki H, Hamamatsu T, Ito S (2004) Appl Phys Lett 84:356

Editor: S. Kobayashi